

RESEARCH ARTICLE | SEPTEMBER 25 2023

# Identification of solidification cracking using multiple sensors and deep learning in laser overlap welded Al 6000 alloy FREE

Special Collection: [Proceedings of the International Congress of Applications of Lasers & Electro-Optics \(ICALEO 2023\)](#)

Jeonghun Shin ; Sanghoon Kang ; Cheolhee Kim ; Sukjoon Hong ; Minjung Kang  



*J. Laser Appl.* 35, 042019 (2023)  
<https://doi.org/10.2351/7.0001112>



CrossMark

### Articles You May Be Interested In

Influences of cracking of coated superconducting layer on voltage-current curve, critical current, and n - value in DyBCO-coated conductor pulled in tension

*J. Appl. Phys.* (September 2010)

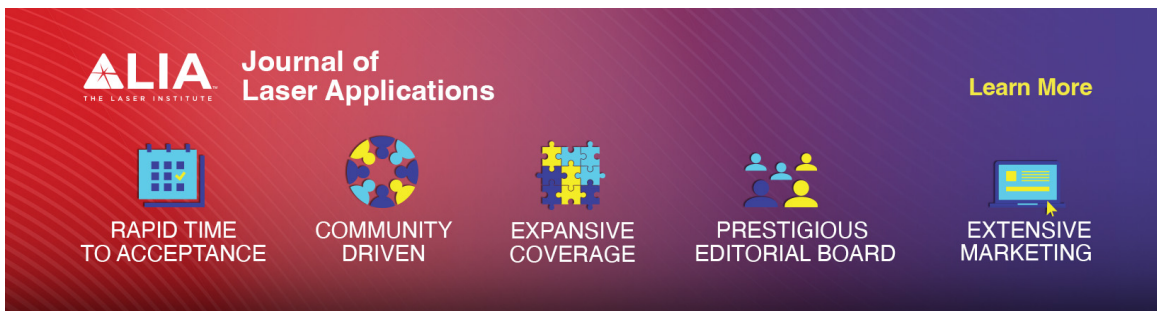
Noninvasive tracking of solidification using ultrasound

*J Acoust Soc Am* (October 2022)

Semisolid solidification of high temperature superconducting oxides

*Journal of Applied Physics* (July 1992)

01 October 2023 07:38:03



**ALIA** THE LASER INSTITUTE **Journal of Laser Applications** [Learn More](#)

- RAPID TIME TO ACCEPTANCE**
- COMMUNITY DRIVEN**
- EXPANSIVE COVERAGE**
- PRESTIGIOUS EDITORIAL BOARD**
- EXTENSIVE MARKETING**

# Identification of solidification cracking using multiple sensors and deep learning in laser overlap welded Al 6000 alloy

Cite as: J. Laser Appl. 35, 042019 (2023); doi: 10.2351/7.0001112

Submitted: 26 June 2023 · Accepted: 1 September 2023 ·

Published Online: 25 September 2023



Jeonghun Shin,<sup>1,2</sup> Sanghoon Kang,<sup>1</sup> Cheolhee Kim,<sup>1</sup> Sukjoon Hong,<sup>2</sup> and Minjung Kang<sup>1,a)</sup>

## AFFILIATIONS

<sup>1</sup>Advanced Joining and Additive Manufacturing R&D Department, Korea Institute of Industrial Technology, Incheon 21999, Korea

<sup>2</sup>Department of Mechanical Engineering, BK21 FOUR ERICA-ACE Center, Hanyang University, Ansan 15588, Korea

**Note:** Paper published as part of the special topic on Proceedings of the International Congress of Applications of Lasers & Electro-Optics 2023.

<sup>a)</sup>Author to whom correspondence should be addressed; electronic mail: kmj1415@kitech.re.kr

## ABSTRACT

Solidification cracking, one of the most critical weld defects in laser welding of Al 6000 alloys, occurs at the final stage of solidification owing to shrinkage of the weld metal and deteriorates the joint strength and integrity. The filler metal can control the chemical composition of the weld metal, which mitigates solidification cracking. However, the chemical composition is difficult to control in autogenous laser welding. Temporal and spatial laser beam modulations have been introduced to control solidification cracking in autogenous laser welding because weld morphology is one of the factors that influences the initiation and propagation of solidification cracking. Solidification cracks generate thermal discontinuities and visual flaws on the bead surface. In this study, a high-speed infrared camera and a coaxial charge-coupled device camera with an auxiliary illumination laser (808 nm) were employed to identify solidification cracking during laser welding. Deep learning models, developed using two sensor images of a solidified bead, provided location-wise crack formation information. The multisensor-based convolutional neural network models achieved an impressive accuracy of 99.31% in predicting the crack locations. Thus, applying deep learning models expands the capability of predicting solidification cracking, including previously undetectable internal cracks.

Key words: Al alloy, laser welding, solidification cracking, deep learning, IR camera, CCD camera

Published under an exclusive license by Laser Institute of America. <https://doi.org/10.2351/7.0001112>

## I. INTRODUCTION

With increasing applications of Al alloys in automotive bodies to satisfy the increasing demand for lightweight automobiles, Al 6000 alloys are increasingly being employed in various car body components owing to their excellent strength and formability.<sup>1-4</sup> However, fusion welding of Al alloys can lead to solidification cracking during the final stage of weld pool solidification when the solid fraction in the mushy zone approaches 1. Crack susceptibility in Al fusion welding is influenced by the chemical composition of the weld metal, with the highest sensitivity occurring when the solute content ranges between 0 and 6 wt.%.<sup>5-10</sup> Pure and highly alloyed Al alloys are less prone to solidification cracking because of the absence of low-melting-point eutectics in pure Al alloys and

the presence of sufficient eutectic liquid in highly alloyed Al alloys, which helps prevent cracking during solidification.<sup>11</sup> Unfortunately, Al 6000 alloys have chemical compositions that render them susceptible to solidification cracking.<sup>12</sup>

Although filler metal is commonly added to mitigate solidification cracking in fusion welding,<sup>13</sup> its application is limited to autogenous laser welding, in which no filler metal is supplied. As an alternative approach, temporal and spatial laser beam modulations have been proposed. Zigzag weaving has been shown to reduce solidification crack propagation by reducing the effective restraint force.<sup>14,15</sup> Weld morphology is another factor that influences crack propagation during laser weave welding. In zigzag weave laser welding, a curvilinear columnar dendritic

01 October 2023 07:38:03

microstructure develops along the laser trajectory, while a narrow equiaxed grain zone along the centerline can help prevent solidification cracking.<sup>16</sup> High-speed beam scanners have enabled the implementation of various laser welding patterns. Kang *et al.*<sup>17</sup> demonstrated that the width of the center equiaxed grain zone could be oscillated longitudinally by selecting appropriate combinations of welding speeds and beam patterns, effectively hindering crack propagation.<sup>17</sup> In addition, ring-core multibeam lasers<sup>18</sup> and partial penetration welding<sup>19</sup> have been found to reduce the solidification cracking susceptibility in the laser welding of Al 6000 alloys.

Despite progress in crack mitigation research, solidification cracking in Al 6000 alloys has not been completely eliminated, necessitating the prediction and inspection of cracks to ensure weld quality. Surface solidification cracks are easily observable, but detecting internal solidification cracks requires special tests such as x-ray, ultrasonic, or destructive tests. Unfortunately, these tests are time-consuming, expensive, and require specialized equipment. Therefore, there is a need for nondestructive, easy-to-apply, and inline crack prediction and inspection technologies in the automotive industry to enhance safety and quality while reducing cost and time.

Recently, the integration of deep learning models into welding research has gained attention, with various studies published on the real-time prediction of welding phenomena. Convolutional neural networks (CNNs) have demonstrated the ability to extract characteristic features from images and signals, resulting in an increasing number of publications utilizing CNN models with camera images and time-series signals as inputs for real-time modeling.<sup>20,21</sup> In laser welding, high-speed cameras,<sup>22–24</sup> charge-coupled device (CCD)/complementary metal oxide semiconductor cameras,<sup>25,26</sup> photodiodes,<sup>22,24,27</sup> spectrometers,<sup>22,26</sup> infrared (IR) cameras,<sup>28</sup> and optical coherence tomography sensors<sup>29,30</sup> have been employed as input sensors for deep learning models to predict the weld quality, porosity, penetration depth, and spatter generation. However, even in deep learning modeling, solidification cracks have been identified using weld surfaces<sup>31</sup> and x-ray images rather<sup>32</sup> than real-time images or signals.

The morphology of solidified welds is governed by the thermal history during the solidification. Previous studies have demonstrated that image sensors equipped with auxiliary illumination can distinguish weld pool boundaries from solidified welds, but are unable to capture the temperature profile. High-temperature IR cameras can digitize the temperature profile near the solidification temperature, and affordable IR cameras with sampling rates exceeding 1 kHz are now available. In this study, deep learning models were employed to estimate the occurrence of solidification cracking using images captured by CCD and IR cameras as inputs. The crack locations were identified by analyzing the x-ray images, which revealed both internal and surface cracks. Deep learning models have been developed and evaluated for individual sensors and multisensor setups.

## II. EXPERIMENTAL SETUP

The basic materials used in the experiments were an Al 6014 alloy with a thickness of 1.0 mm and an Al 6016 alloy with a thickness of 1.8 mm, the chemical compositions of which are listed in

TABLE I. Chemical composition of materials (wt. %).

Alloy	Al	Si	Fe	Cu	Mn	Mg	Cr	Ti
Al 6014	98.27	0.60	0.23	0.13	0.08	0.65	0.01	0.03
Al 6016	98.63	1.00	0.19	0.03	0.07	0.40	0.01	0.03

Table I. The specimens were cut and machined into sheets with dimensions of 100 and 30 mm in length and width, respectively. An Al 6014 sheet was fully overlapped with an Al 6016 sheet for welding.

A Yb:YAG disk laser (TruDisk 3002, Trumpf Laser GmbH, Schramberg, Germany) with a wavelength of 1030 nm was employed as a laser beam generation source and delivered through an optical fiber with a diameter of 0.2 mm and a focusing optic with a focal distance of 560 mm. The laser beam was focused on the top surface of the specimens with a diameter of 0.54 mm. Two image sensors were employed to gather the inputs for the deep learning models [Fig. 1(a)]. A CCD camera (UI-3140CP Rev. 2, iDS, Obersulm, Germany) was coaxially installed on the focusing optics, and the resolution and sampling rate were  $864 \times 320$  pixels and 250 fps, respectively. An illumination laser was used to monitor the laser keyhole, weld pool, and solidified bead shape simultaneously. The wavelength and power of the illuminating laser were 808 nm and 30 W, respectively. A bandpass filter with an  $808 \pm 5$  nm band was attached to the front of the CCD camera. An IR camera (TACHYON 16k+, NIT, Madrid, Spain) was set up off-axis with a resolution and sampling rate of  $128 \times 128$  pixels and 500 fps, respectively.

A welding trial was conducted with a weld length of 80 mm at the center of the specimens using a one-axis traveling system [Fig. 1(b)]. Both sides of the specimens were fixed at a constraint length of 10 mm, which was consistently applied in all the welding trials. The laser power ranged from 2.6 to 3.0 kW in increments of 0.1 kW, while the travel speed ranged from 1.0 to 3.0 m/min in increments of 0.5 m/min (Table II). A total of 25 conditions were implemented to cover all combinations.

After welding, the specimens underwent x-ray testing for inspection (Fig. 2). The digitized x-ray test results had a resolution of  $1125 \times 420$  pixels. Gray levels within a mask of 80 pixels in the width direction and 1 pixel in the length direction at the longitudinal centerline were examined along the weld line. When the sixth brightest pixel had a gray level higher than 170, the point was coded as 1 (crack); otherwise, it was coded as 0 (noncrack).

Welded specimens were prepared to observe the microstructure along the plane normal to the sheet surface. The samples were polished and etched in a solution containing 100 ml chilled water, 2.5 ml HCl, 1.5 ml HNO<sub>3</sub>, and 1 ml HF. The microstructure was analyzed using optical microscopy (CX40M, Sunny Korea, Busan, Korea) and field-emission scanning electron microscopy (FE-SEM, JSM-IT800, JEOL, Tokyo, Japan). The electron backscatter diffraction (EBSD, Symmetry S3, Oxford Instruments, Abingdon, UK) data were acquired using a FE-SEM system. Before EBSD analysis, the coupons were mechanically polished using colloidal silica to avoid etching the edges of the cracks. A high-angle grain boundary (HAGB) is defined as a boundary misorientation greater than 15°,

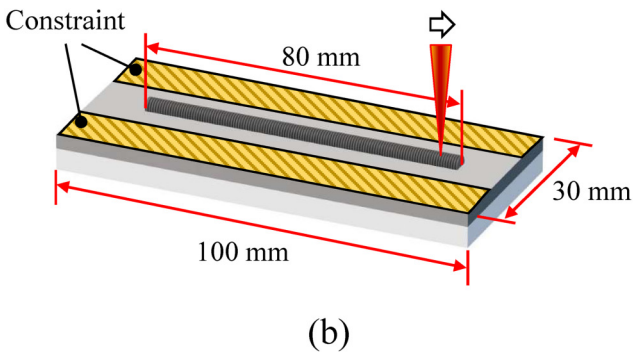
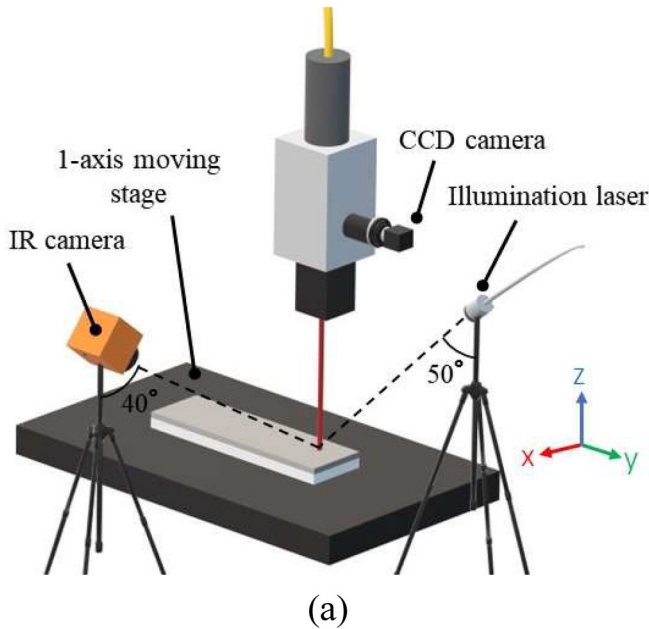


FIG. 1. Experimental setup configuration of (a) data acquisition system and (b) jig fixture.

and the structure is defined as a feature of grains enclosed by the HAGB.

### III. MODELS AND DATA PREPARATION

Three CNN models were constructed to predict the crack occurrence using the CCD and IR camera images (Fig. 3). In the

TABLE II. Applied welding parameters.

Welding parameter (unit)	Value (levels)
Laser power (kW)	2.6–3.0 (5)
Welding speed (m/min)	1.0–3.0 (5)
Focal position (mm)	0 (1)

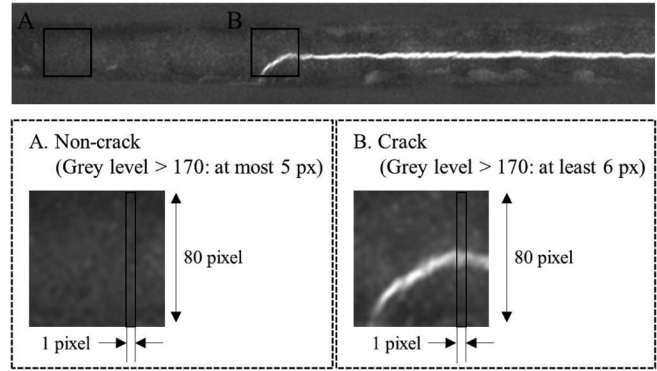


FIG. 2. X-ray image processing to define the hot crack location.

multi-input model, single-input models using CCD and IR camera images were combined, and the structure was similar to that of the single-input models. Features were extracted through two CNN blocks: convolution, batch normalization, and max pooling layers, and crack occurrence was classified into two dense (fully connected) layers. The activation function was a rectified linear unit function, except for the output node, whose activation function was a sigmoid function.

The two IR images were averaged, and the IR and CCD images were synchronized at a sampling rate of 250 Hz. Totally, 12 500 data points were prepared regardless of the welding

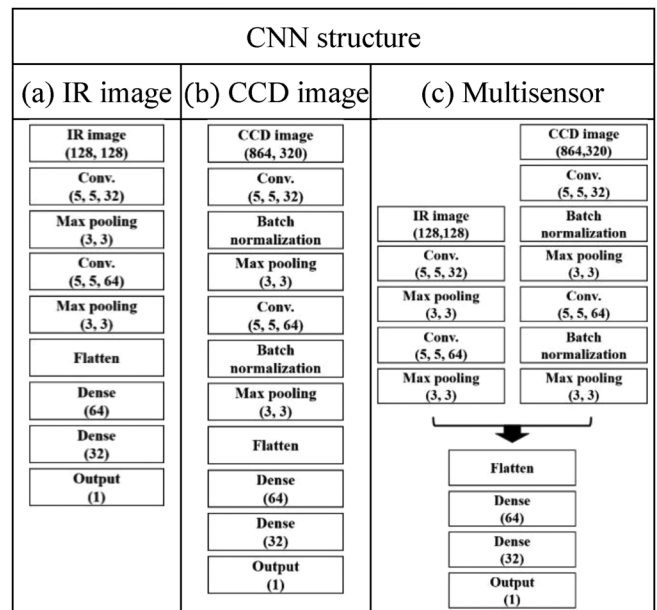


FIG. 3. Deep learning model structure: (a) IR image, (b) CCD image, and (c) multisensor.

01 October 2023 07:38:03

TABLE III. Data groups according to crack detection.

	Cracking detection by		
	CCD	Appearance	X ray
Group 1	No	No	No
Group 2	No	No	Yes
Group 3	No	Yes	Yes
Group 4	Yes	Yes	Yes

conditions. The data points were divided into training, validation, and test data points at a ratio of 70:15:15.

During training, the binary cross-entropy function was chosen as the loss function, and the Adam optimizer was applied using the default parameters proposed by Kingma and Ba,<sup>33</sup> namely, learning rate of  $10^{-3}$ ,  $\beta_1 = 0.9$ ,  $\beta_2 = 0.999$ , and  $\epsilon = 10^{-8}$ . Here,  $\beta_1$  and  $\beta_2$  are the exponential decay rates for the first- and second-moment estimates, respectively, and  $\epsilon$  is a low-valued constant that prevents division by zero. The models were trained for 300 epochs in mini-batches of 16 samples.

#### IV. RESULTS

##### A. Welding phenomena and cracking behavior

Analyzing the temperature field surrounding the welds and monitoring the movement of the solid-liquid interface can help predict the locations of hot cracks. The surrounding stress field (restraint), cooling rate, and weld morphology are a few factors that affect hot cracking. The cooling rate ( $dT/dt$ ) was calculated by multiplying the temperature gradient ( $G$ ,  $dT/dl$ ) by the solidification rate ( $R$ ,  $dl/dt$ ), where  $T$ ,  $t$ , and  $l$  denote the temperature, time, and location, respectively. The weld morphology was determined by the ratio of  $G$  to  $R$ . By examining the temperature field obtained through the IR camera and the molten pool images captured by the CCD sensor, it was possible to estimate the behavior of hot cracking. Compared to the IR camera, the CCD sensor used in the experiment provided a higher resolution for observing the motion of the liquidus and identifying surface roughness and surface cracks.

IR and CCD images were acquired during the laser welding and synchronized with the captured bead appearance and x-ray photographs. The heat input per unit length varied between 52 and 180 J/mm. The data points were categorized into four groups based on the crack observations (Table III), and representative images are presented in Fig. 4.

As the heat input increased, the CCD and IR images revealed expansion of the molten pool. When the crack width was relatively small [Fig. 4(b)], the crack was only visible in the x-ray image and not in the bead or CCD images. As the crack width increased, it became visible in the bead appearance and x-ray image [Fig. 4(c)]. With further widening, cracks could also be observed in the CCD images [Fig. 4(d)].

The crack and noncrack locations were counted at intervals of 10 J/mm as the heat input. For example, the crack count at 50 J/mm represents the number of crack locations observed when

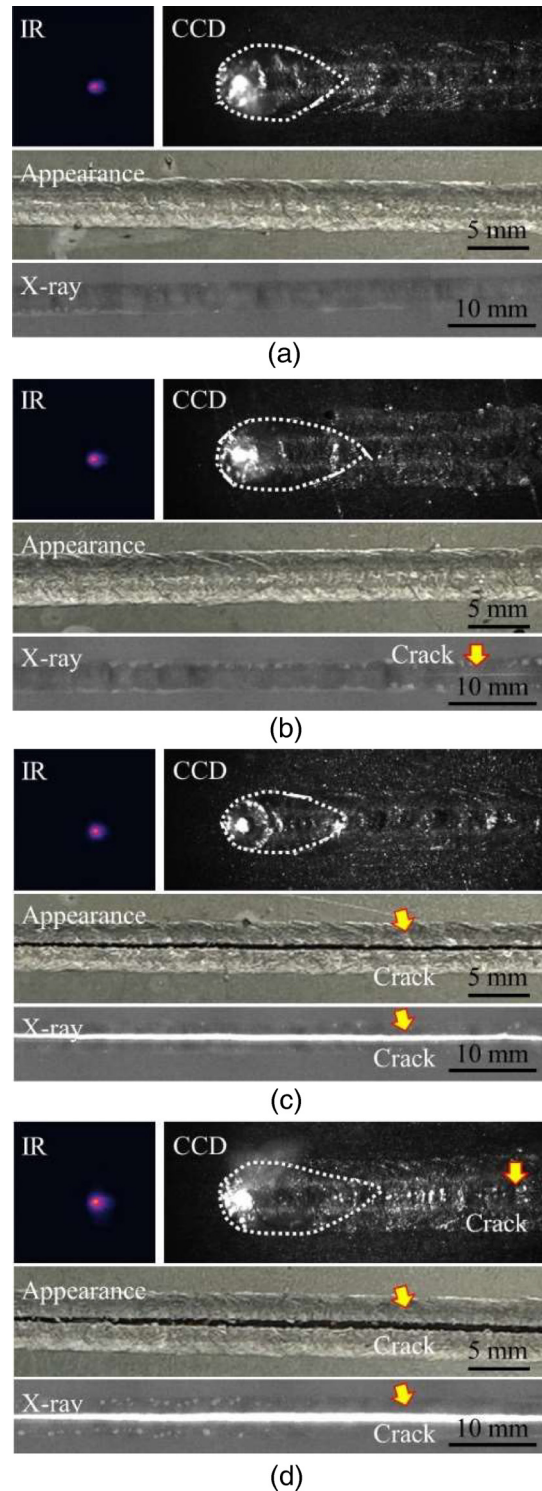


FIG. 4. Representative data set based on group with various heat input: (a) group 1: 112 J/mm, (b) group 2: 116 J/mm, (c) group 3: 90 J/mm, and (d) group 4: 120 J/mm.

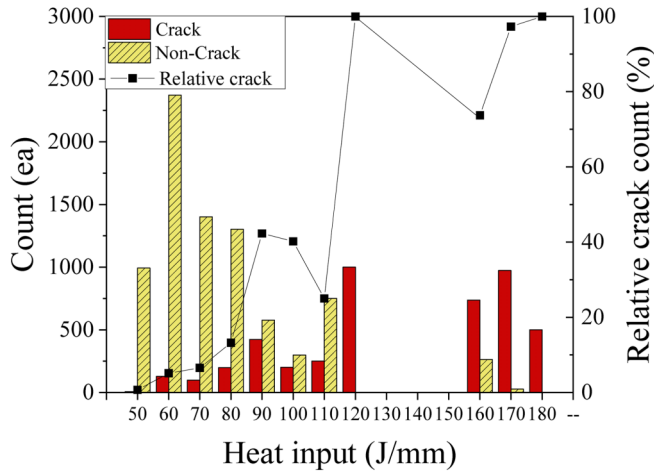


FIG. 5. Crack count in the data set according to the heat input.

the heat input ranges from 45 to 55 J/mm. Because the number of data points within each range varied depending on the heat input, the relative crack count is also included in Fig. 5. Increasing the heat input per unit length led to an increase in the relative crack

count. This can be attributed to the higher thermal deformation during cooling and the increased restraint force exerted on the welds as the heat input increased.

The crack behavior and microstructural evolution in relation to the heat input are shown in Fig. 6. The central region of the welds predominantly exhibits an equiaxed structure, whereas a columnar dendritic structure forms near the fusion line. Under all the conditions, the cracks propagated along the grain boundaries of the equiaxed structure. However, the crack path that was initially curvilinear at the lowest heat input [Fig. 6(a)] became straighter as the heat input increased [Figs. 6(b) and 6(c)]. The grain size increased proportionally with heat input, as shown in Figs. 6 and 7. For a low heat input of 89.1 J/mm, the grain size distribution exhibited the highest frequency around 100 μm, whereas it shifted to approximately 170 and 210 μm for the intermediate (120.0 J/mm) and high (156.0 J/mm) heat input cases, respectively. The curvilinear crack path observed at lower heat inputs can be attributed to the smaller grain size and, consequently, the shorter crack propagation distance.

### B. Model training and test results

The training process for the CCD image and multisensor models successfully avoided overfitting and reached saturation within 300 epochs. However, the IR image model exhibited a slight

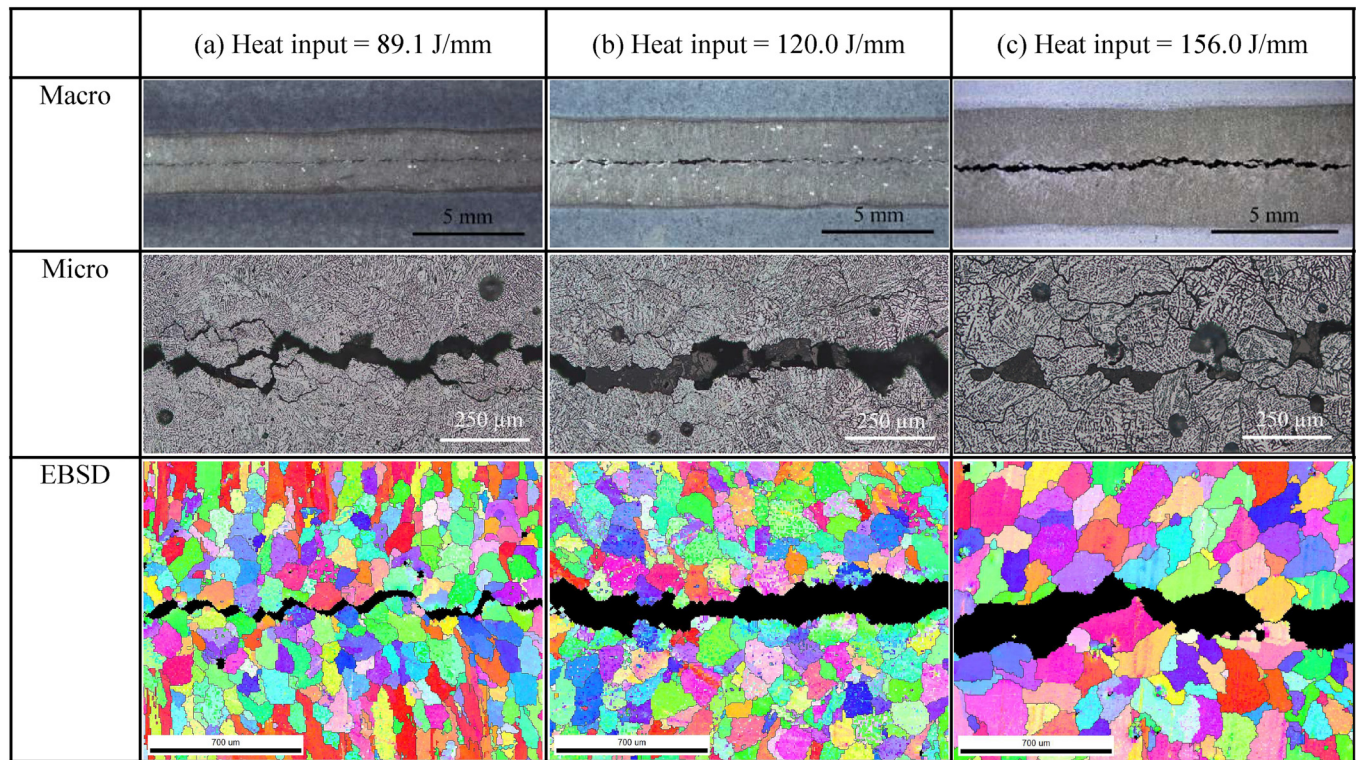


FIG. 6. Magnified weld bead surfaces and their EBSD images.

01 October 2023 07:38:03

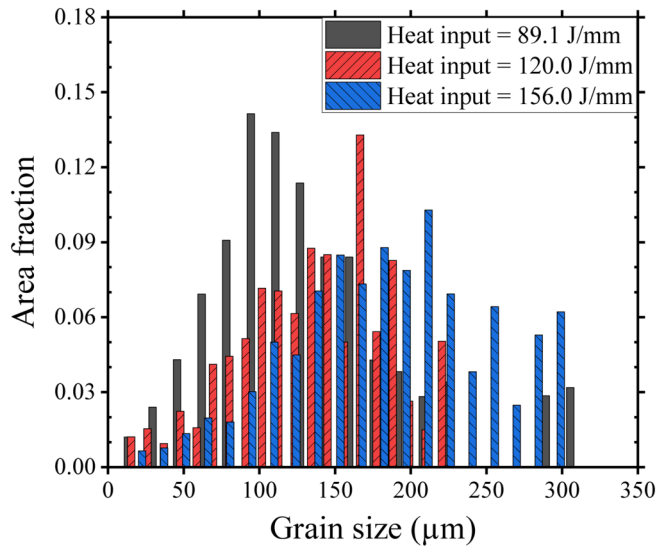


FIG. 7. Grain size distribution in the central region of welds according to heat input.

overfitting after only ten epochs (Fig. 8). This overfitting tendency can be attributed to the lower resolution of the IR image and the small object area within the image. To mitigate overfitting, it is recommended to increase the resolution of the IR image or consider image magnification techniques to provide a larger and more detailed representation of the objects in the image.

The three models exhibited excellent performance in predicting crack locations, as evidenced by the confusion matrix shown in Fig. 9. The accuracies of the test models were 96.48%, 98.77%, and 99.31% for the IR, CCD, and multisensor models, respectively (Table IV). The multisensor utilizing both sensor feature extractions exhibited the best performance. Among the 1875 data points, incorrect prediction was carried out at only 13 data points. Moreover, cracking is a locally continuous phenomenon, so temporal averaging in the model prediction output for successive images can enhance the accuracy of the prediction models. As shown in Fig. 10, an inaccurate prediction, that is, a residual in the modeling, was distributed over the heat input, and a slight concentration was found at 120 J/mm in the IR image model. Inaccurate predictions can be classified into two types: false cracks and false noncracks. False cracks occur when a crack is predicted despite the x-ray image showing no actual crack. Conversely, false noncracks happen if a noncrack is predicted when an actual crack is observed in the x-ray image. Tables V and VI list the number of inaccurate predictions obtained with the CCD image and multisensory models, respectively, categorized according to the groups outlined in Table III. As indicated, group IV did not result in any inaccurate predictions, group I contained only false cracks, and groups II and III included solely false noncracks. Notably, the number of inaccurate predictions in group III significantly decreased from the CCD to the multisensory model.

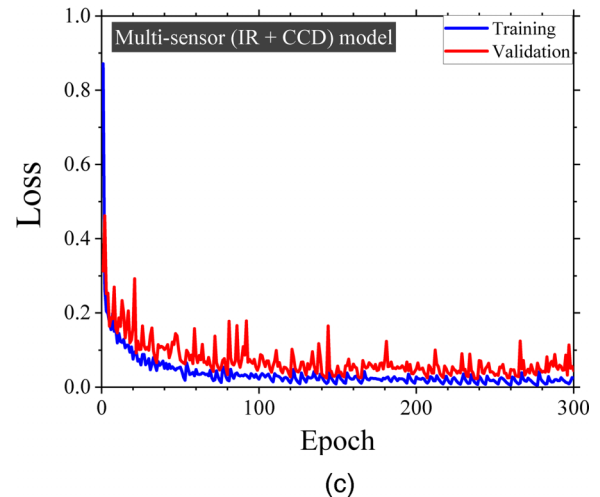
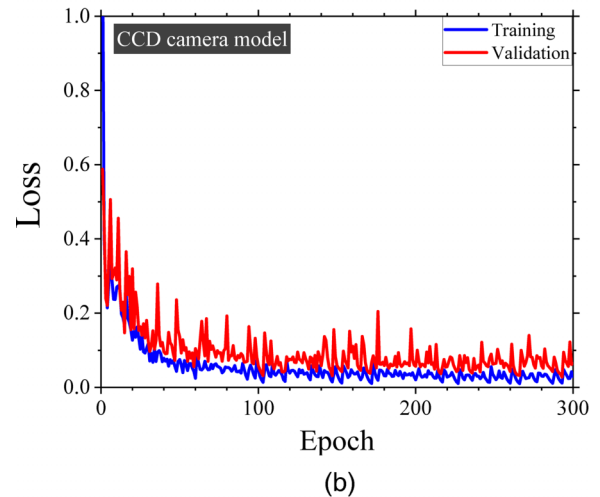
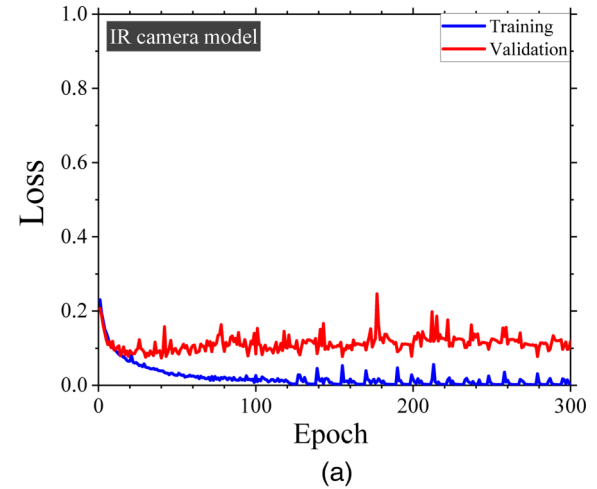


FIG. 8. Training and validation losses for (a) the IR image model, (b) the CCD image model, and (c) the multisensor model.

01 October 2023 07:38:03

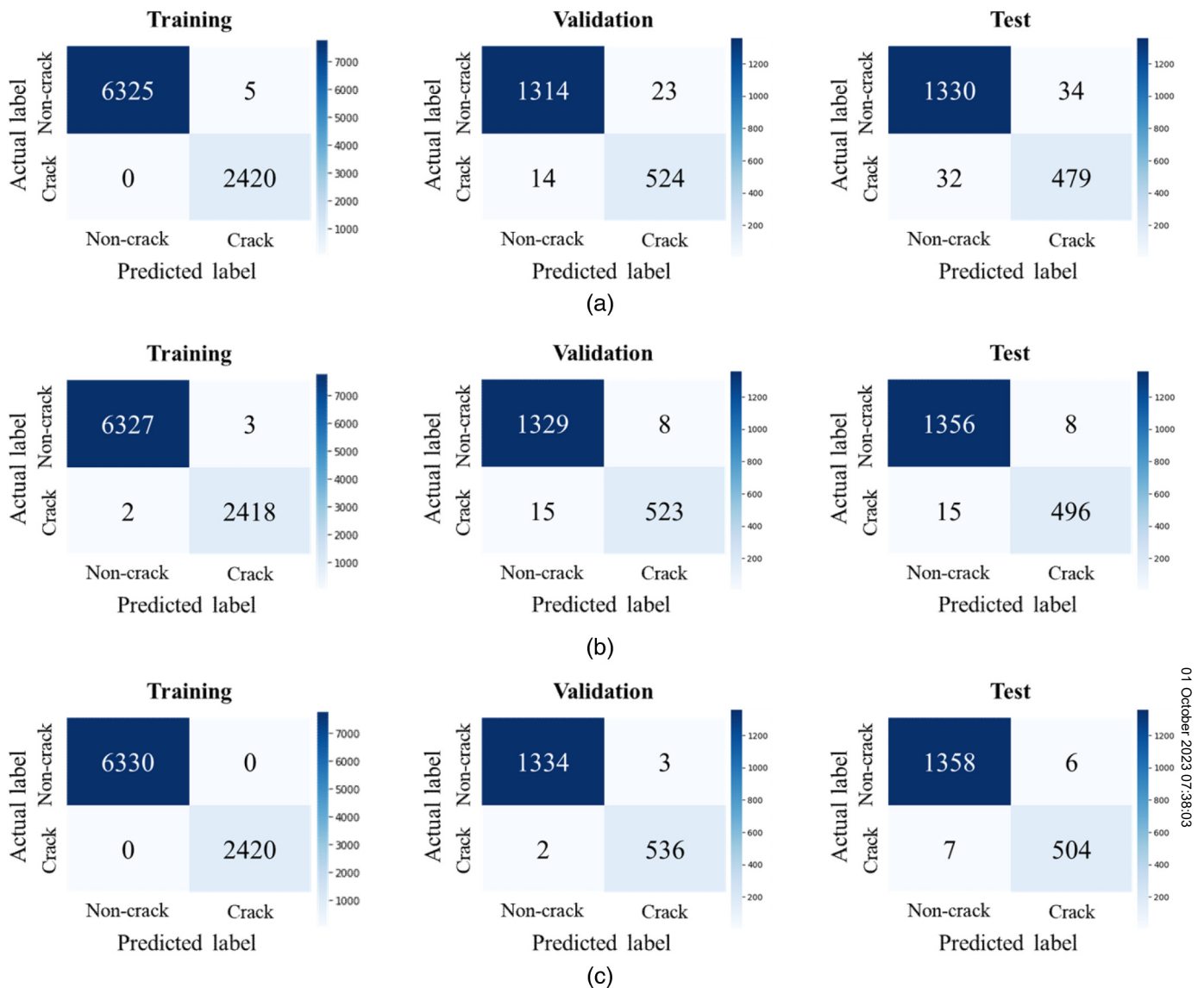


FIG. 9. Confusion matrix obtained with the (a) IR image, (b) CCD image, and (c) multisensor models.

### V. DISCUSSION

The present study successfully developed deep learning models capable of predicting crack locations with remarkable precision, reaching accuracies of up to 99.31% during model testing. The training data set used comprised 12 500 CCD and IR images sampled at 250 Hz.

Previous research on machine learning models for laser welding has provided valuable insights into classifying and predicting welding characteristics. For example, a combination of photodiodes, spectrometers, and high-speed cameras effectively detected geometric weld defects.<sup>22</sup> Other investigations utilized either near

IR and midwave IR cameras,<sup>28</sup> or optical coherence tomography<sup>29,30</sup> to identify geometric defects. The penetration mode for butt joints was predicted through coaxial high-speed imaging techniques,<sup>23</sup> whereas that for Al/Cu overlap joints has been successfully estimated using photodiodes<sup>27</sup> or a combination of photodiodes and high-speed cameras.<sup>24</sup> Depth estimation was also accomplished through a combination of spectrometer signals and CCD images.<sup>26</sup>

Solidification cracking is influenced by various metallurgical factors, including the stress induced by constrained thermal shrinkage. Camera images can digitize and detect essential geometric

01 October 2023 07:38:03



TABLE IV. Prediction accuracy of different models.

Model	Accuracy (%)		
	Training data	Validation data	Test data
IR image	99.94	98.03	96.48
CCD image	99.94	98.77	98.77
Multisensor	100	99.73	99.31

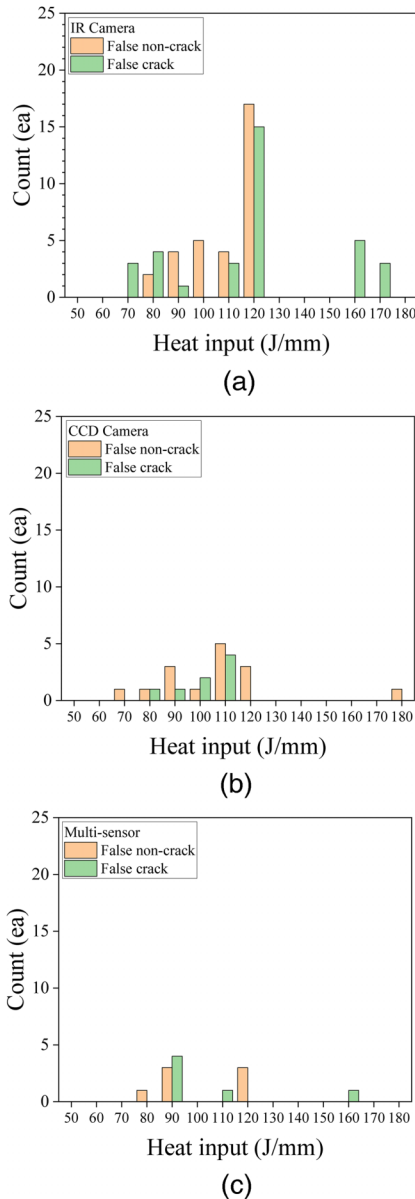


FIG. 10. Residual analysis based on crack count: (a) the IR camera input model, (b) the CCD camera input model, and (c) the multisensor input model.

features such as welding pools and keyhole shapes. Deep learning models based on camera images can also be used to detect concealed geometric features such as penetration modes and depth. Zhang *et al.*<sup>25</sup> expanded on this, noting that weld pool images capture not only the geometric features of weld pools but also the associated flow patterns, rendering them valuable for predicting porosity formation. This study demonstrates the exceptional efficiency of both the CCD image and multisensor models in identifying cracks, which are among the metallurgical features of interest.

Hot cracking occurs when the balance between material resistance and cracking forces is disrupted. This force imbalance emerges during welding processes involving heating and shrinkage and is influenced by the amount of heat input and surrounding restraint. The molten pool expands during heating and contracts during cooling. Therefore, analyzing the relative movement at the tail of the weld pool with respect to the static environment can provide insight into crack susceptibility.

Observations of temperature and deformation distribution in the crack-sensitive region, specifically the tail of the molten pool, offer insight into predicting hot cracks. According to Rappaz's solidification crack criterion,<sup>34</sup> the thermomechanical path of an alloy,  $\epsilon(T)$ , must not intersect the U-shaped ductile curve. The variation of distortion with respect to temperature,  $\partial\epsilon/\partial T = \partial\epsilon/\partial t \times \partial t/\partial T$ , has been used as a hot cracking indicator. This implies that the thermal history ( $\partial T/\partial t$ ) and thermal distortion ( $\partial\epsilon/\partial t$ ) occurring near the tail of the molten pool during solidification, as obtained in this study, play a significant role in predicting hot cracks.

Three crack types were identified (Table III). Group II cracks were located below the weld surface and required x-ray testing, instead of CCD imaging or visual inspection, for detection. Groups III and IV comprised surface cracks. Group IV cracks were visible within the CCD image's field of view, and both the developed CCD and multisensory models accurately detected their formation, as evidenced by Tables V and VI. Group III cracks were beyond the CCD camera's field of view and were not apparent in CCD images. However, both the CCD and multisensory models successfully predicted these group III cracks. The addition of infrared (IR) images to the multisensor model, alongside CCD images, contributed to improving the model's accuracy. As previously explained, IR images encapsulate thermal history, enhancing the performance of the multisensor model in cases like group III where cracks are not directly visible in CCD images. This resulted in reducing false non-crack cases from 9 to 2, compared to the CCD image model.

Among the deep learning models considered in this study, the IR image model demonstrated relatively lower accuracy. As shown in Fig. 4, because of their lower magnification, IR images display smaller weld pool sizes than CCD images. Therefore, by increasing IR image magnification or resolution, the accuracy of both the IR image and multisensory models could be enhanced.

TABLE V. Residual analysis per data group using the CCD image model.

	Group I	Group II	Group III	Group IV
False noncracks	0	6	9	0
False cracks	8	0	0	0

01 October 2023 07:38:03

TABLE VI. Residual analysis per data group using the multisensor model.

	Group I	Group II	Group III	Group IV
False noncracks	0	5	2	0
False cracks	6	0	0	0

## VI. CONCLUSION

Deep learning models were developed to identify the locations of solidification cracks in the laser overlap welding of Al 6000 alloys. IR and CCD camera images were selected as inputs at a sampling rate of 250 Hz, and the crack location identified from the x-ray image was chosen as the output. The following conclusions were drawn using CNN-based deep learning models.

- (1) The developed deep learning model could predict the cracking location with excellent accuracy, and the best prediction with the multisensor input model had an accuracy of 99.31%.
- (2) Solidification cracking occurred because of intergranular cracking along the equiaxed grains in the center of the welds. The multisensor was composed of a low-resolution IR camera that monitored the temperature gradient and a high-resolution CCD camera that estimated solidification.
- (3) The accuracy of the prediction models could be enhanced using higher-resolution sensors and magnifying IR camera images.

This study successfully demonstrated that deep learning models can detect solidification cracking, including internal cracks, using visual and IR camera images.

## ACKNOWLEDGMENTS

We would like to acknowledge the technical and financial from the MOTIE (Ministry of Trade, Industry, and Energy) in Korea (Grant No. 20014809)

## AUTHOR DECLARATIONS

### Conflict of Interest

The authors have no conflicts to disclose.

## Author Contributions

**Jeonghun Shin:** Investigation (equal); Methodology (equal); Software (equal); Writing – original draft (equal). **Sanghoon Kang:** Methodology (equal); Software (equal). **Cheolhee Kim:** Supervision (equal); Writing – original draft (equal); Writing – review & editing (equal). **Sukjoon Hong:** Supervision (equal); Validation (equal). **Minjung Kang:** Conceptualization (equal); Formal analysis (equal); Supervision (equal); Writing – original draft (equal); Writing – review & editing (equal).

## REFERENCES

<sup>1</sup>T. Sakurai, “The latest trends in aluminum alloy sheets for automotive body panels,” *Kobelco Technol. Rev.* **28**, 22–28 (2008).

- <sup>2</sup>Y. Ota, T. Masuda, and S. Kimura, “Technical trends in aluminum alloy sheets for automotive body panels,” *Kobelco Technol. Rev.* **38**, 16–20 (2020).
- <sup>3</sup>G. M. Panã, “Developments of Audi space frame technology for automotive body aluminum construction,” *Appl. Mech. Mater.* **896**, 127–132 (2020).
- <sup>4</sup>W. Zhang and J. Xu, “Advanced lightweight materials for automobiles: A review,” *Mater. Des.* **221**, 110994 (2022).
- <sup>5</sup>A. Singer and P. Jennings, “Hot-shortness of the aluminium-silicon alloys of commercial purity,” *J. Inst. Met.* **73**, 197–212 (1946).
- <sup>6</sup>A. Singer and P. Jennings, “Hot-shortness of some aluminium-iron-silicon alloys of high purity,” *J. Inst. Met.* **73**, 273–284 (1947).
- <sup>7</sup>P. Jennings, A. Singer, and W. Pumphrey, “Hot-shortness of some high-purity alloys in the systems aluminium-copper-silicon and aluminium-magnesium-silicon,” *J. Inst. Met.* **74**, 227–248 (1948).
- <sup>8</sup>W. Pumphrey and J. Lyons, “Cracking during the casting and welding of the more common binary aluminium alloys,” *J. Inst. Met.* **74**, 439–455 (1948).
- <sup>9</sup>J. Dowd, “Weld cracking of aluminum alloys,” *Weld. J.* **31**, 448–456 (1952).
- <sup>10</sup>J. H. Dudas, “Preventing weld cracks in high strength aluminum alloys,” *Weld. J.* **45**, 241–249 (1966).
- <sup>11</sup>S. Kou, *Welding Metallurgy*, 2nd ed. (Wiley, New York, 2002).
- <sup>12</sup>C.-H. Kim, Y.-N. Ahn, and H.-S. Lim, “Laser welding of automotive aluminium alloys,” *J. Weld. Join.* **29**, 21–26 (2011).
- <sup>13</sup>Y. N. Ahn and C. H. Kim, “Evaluation of crack sensitivity and gap bridging ability during laser butt welding of aluminum 5J32 and 6K21 alloys,” *Mater. Sci. Forum* **695**, 247–250 (2011).
- <sup>14</sup>K.-D. Choi, Y.-N. Ahn, and C. Kim, “Weld strength improvement for Al alloy by using laser weaving method,” *J. Laser Appl.* **22**, 116–119 (2010).
- <sup>15</sup>B. H. Kim, N. H. Kang, W. T. Oh, C. H. Kim, J. H. Kim, Y. S. Kim, and Y. H. Pari, “Effects of weaving laser on weld microstructure and crack for Al 6k21-T4 alloy,” *J. Mater. Sci. Technol.* **27**, 93–96 (2011).
- <sup>16</sup>C. Kim, M. Kang, and N. Kang, “Solidification crack and morphology for laser weave welding of Al 5J32 alloy,” *Sci. Technol. Weld. Join.* **18**, 57–61 (2013).
- <sup>17</sup>M. Kang, H. Han, and C. Kim, “Microstructure and solidification crack susceptibility of Al 6014 molten alloy subjected to a spatially oscillated laser beam,” *Materials* **11**, 648 (2018).
- <sup>18</sup>M. Kang and C. Kim, “Evaluation of hot cracking susceptibility on laser welded aluminum alloy using coaxially arranged multiple-beam laser,” *J. Laser Appl.* **32**, 022072 (2020).
- <sup>19</sup>M. Kang, J. Cheon, D. H. Kam, and C. Kim, “The hot cracking susceptibility subjected the laser beam oscillation welding on 6XXX aluminum alloy with a partial penetration joint,” *J. Laser Appl.* **33**, 012032 (2021).
- <sup>20</sup>K. Lee, S. Yi, S. Hyun, and C. Kim, “Review on the recent welding research with application of CNN-based deep learning—Part I: Models and applications,” *J. Weld. Join.* **39**, 10–19 (2021).
- <sup>21</sup>K. Lee, S. Yi, S. Hyun, and C. Kim, “Review on the recent welding research with application of CNN-based deep learning—Part II: Model evaluation and visualizations,” *J. Weld. Join.* **39**, 20–26 (2021).
- <sup>22</sup>Y. Zhang, D. You, X. Gao, N. Zhang, and P. P. Gao, “Welding defects detection based on deep learning with multiple optical sensors during disk laser welding of thick plates,” *J. Manuf. Syst.* **51**, 87–94 (2019).
- <sup>23</sup>Z. Zhang, B. Li, W. Zhang, R. Lu, S. Wada, and Y. Zhang, “Real-time penetration state monitoring using convolutional neural network for laser welding of tailor rolled blanks,” *J. Manuf. Syst.* **54**, 348–360 (2020).
- <sup>24</sup>S. Kang, K. Lee, M. Kang, Y. H. Jang, and C. Kim, “Weld-penetration-depth estimation using deep learning models and multisensor signals in Al/Cu laser overlap welding,” *Opt. Laser Technol.* **161**, 109179 (2023).
- <sup>25</sup>B. Zhang, K.-M. Hong, and Y. C. Shin, “Deep-learning-based porosity monitoring of laser welding process,” *Manuf. Lett.* **23**, 62–66 (2020).
- <sup>26</sup>S. Kang, M. Kang, Y. H. Jang, and C. Kim, “Deep learning-based penetration depth prediction in Al/Cu laser welding using spectrometer signal and CCD image,” *J. Laser Appl.* **34**, 042035 (2022).
- <sup>27</sup>K. Lee, S. Kang, M. Kang, S. Yi, and C. Kim, “Estimation of Al/Cu laser weld penetration in photodiode signals using deep neural network classification,” *J. Laser Appl.* **33**, 042009 (2021).

- <sup>28</sup>C. Knaak, J. von Eßen, M. Kröger, F. Schulze, P. Abels, and A. Gillner, “A spatio-temporal ensemble deep learning architecture for real-time defect detection during laser welding on low power embedded computing boards,” *Sensors* **21**(12), 4205 (2021).
- <sup>29</sup>C. Stadter, M. Schmoeller, L. von Rhein, and M. F. Zaeh, “Real-time prediction of quality characteristics in laser beam welding using optical coherence tomography and machine learning,” *J. Laser Appl.* **32**, 022046 (2020).
- <sup>30</sup>T. Brežan, P. Franciosa, M. Jezeršek, and D. Ceglarek, “Fusing optical coherence tomography and photodiodes for diagnosis of weld features during remote laser welding of copper-to-aluminum,” *J. Laser Appl.* **35**, 012018 (2023).
- <sup>31</sup>C. V. Dung, H. Sekiya, S. Hirano, T. Okatani, and C. Miki, “A vision-based method for crack detection in gusset plate welded joints of steel bridges using deep convolutional neural networks,” *Automat. Constr.* **102**, 217–229 (2019).
- <sup>32</sup>B. Gao, H. Zhao, X. Miao, and T. Wu, “Quality assessment algorithm of x-ray images in overall girth welds based on deep neural network,” *J. Pipeline Syst. Eng. Practice* **14**, 04022073 (2023).
- <sup>33</sup>D. P. Kingma and J. Ba, “Adam: A method for stochastic optimization,” *arXiv:1412.6980* (2014).
- <sup>34</sup>M. Rappaz, J.-M. Drezet, and M. Gremaud, “A new hot-tearing criterion,” *Metall. Mater. Trans. A* **30**, 449–455 (1999).